

NANO-STRUCTURED PLASMONIC SENSORS AND DEVICES

AJAY KUMAR AGRAWAL



**DEPARTMENT OF ELECTRICAL ENGINEERING
INDIAN INSTITUTE OF TECHNOLOGY DELHI**

APRIL 2022

© Indian Institute of Technology Delhi (IITD), New Delhi, 2022

NANO-STRUCTURED PLASMONIC SENSORS AND DEVICES

by

AJAY KUMAR AGRAWAL

Department of Electrical Engineering

Submitted

in fulfillment of the requirements of the degree of

Doctor of Philosophy

to the



INDIAN INSTITUTE OF TECHNOLOGY DELHI

APRIL 2022

Dedication

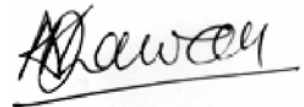
*To my loving father, Suresh Kumar Agrawal, and
to my joyful and kind grandmother, Keshar Devi*

and

To the memory of my mother, Usha Devi

CERTIFICATE

This is to certify that the thesis entitled “Nano-structured Plasmonics sensors devices” being submitted by **Mr. Ajay Kumar Agrawal** to the **Indian Institute of Technology Delhi**, for the award of the degree of **Doctor of Philosophy** in the Department of Electrical Engineering, is a record of bonafide research work carried out by him. Mr. Ajay Kumar Agrawal has worked under my guidance and supervision and has fulfilled the requirements for the submission of this thesis, which to my knowledge has reached the requisite standard. The results contained in this thesis have not been submitted in part or in full to any other University or Institute for the award of any degree or diploma.



Prof. Anuj Dhawan

(Supervisor)

Department of Electrical Engineering

Indian Institute of Technology Delhi

New Delhi, 110016, India.

ACKNOWLEDGEMENTS

I want to thank and express my gratitude to my supervisor Prof. Anuj Dhawan for his valuable guidance and support during my Ph.D. I am grateful to him for sharing his immense knowledge that has helped me during my research. His continuous motivation and generous support have been the driving force to complete my Ph.D. work.

I would also thank all my SRC faculty members, Prof. Swades De, Prof. Manan Suri, and Prof. P. K. Muduli, for their support during my research. I would also like to thank the faculty members and staff members of the department of electrical engineering at IIT Delhi.

I want to thank all the colleagues and friends working with me in the laboratory; Kamal Kumar, Uttam Kumar, Priten Savaliya, Nitin Gupta, Abhijit Das, Kaleem Ahmad, Akanksha Ninawe, Merbin John, Mangesh Jaiswal, and Sanjit Varma for their time and support during my Ph.D. I would also like to thank all my friends in IIT Delhi for their valuable support.

Now, I acknowledge my parents Suresh Kumar Agrawal and Usha Devi, and my grandmother Keshar Devi for their constant and unconditional support during my studies. I would not be where I am today without them being in my life.

Ajay Kumar Agrawal
Ajay Kumar Agrawal
April 2022

New Delhi

ABSTRACT

Nano-structured plasmonic metals have been extensively researched for advances in plasmonic sensors and various optical devices. Nano-structured plasmonic metals enable the excitation of hybrid surface plasmons, which consist of both localized as well as propagation surface plasmons. Localized surface plasmon based devices can be used to detect a local change in the surrounding medium. Nano-structured plasmonic metals enable us to use the coupling technologies of the propagating surface plasmon polariton as well as detection capabilities of the localized surface plasmons.

A surface plasmon resonance sensing and imaging platform based on plasmonic non-uniform nano-gratings with narrow groove is presented. When the localized refractive index of the medium around the gold layer present in these nano-gratings is changed, theoretical analysis is used to numerically compute reflectance and differential reflectance signals. The binding of biomolecules to the gold layer will cause a change in the localized refractive index. Finite difference time domain modeling is used to investigate plasmonic non-uniform nano-gratings. These plasmonic non-uniform nano-gratings provide very high differential reflectance amplitude values.

We also present a theoretical study of the various nano-structured plasmonic sensor chips investigated utilizing the Kretschmann configuration for highly sensitive localized sensing with high tunability from visible to infrared wavelengths. The proposed nano-structured sensor chips are analyzed, and their sensing capability is compared using the rigorous coupled-wave analysis method. The sensitivity parameters are defined to focus on the detection of a thin layer of biomolecules on the surface of nano-structures. Shifts in the reflectivity minima are determined to obtain information on perturbations in localized (local binding analyte layer sensing) and bulk refractive index (bulk medium sensing) on the sensor surface. The dimensions of the nano-structures and the incident angle shift the plasmon resonance wavelengths and can be used to tune the operating wavelength. The nano-structured films create local regions of high electric fields, which results in enhanced sensitivity of the proposed structures. We have then introduced a spacer between the nano-structures and thin film to further enhance the localized sensitivity. The proposed sensors do not require any sophisticated optical set-ups and can be implemented on the optical setups used for the conventional Kretschmann configuration-based sensors. The

proposed sensor design could easily be fabricated using the state-of-the-art top-down nanofabrication approaches and could be employed for developing highly sensitive biosensing platforms. The proposed sensors can be used in surface plasmon resonance imaging (SPRi) to detect multiple biomolecules in a single measurement.

The capability of plasmonic nano-structures to detect localized changes in the surrounding medium is also utilized to design a plasmonic switch. We present plasmonic switches — based on gold nanoparticles (Au NPs) embedded between layers of VO₂ films. Vanadium dioxide (VO₂) undergoes a reversible phase change, from semiconducting to metallic, with a change in temperature. The operating wavelength of the switching device can be tuned between 650 nm and 1000 nm using the localized surface plasmon resonance (LSPR) properties of the Au NPs. We also demonstrate experimentally and theoretically a higher switchability — i.e. a higher extinction ratio upon phase transition of VO₂ — than what has been shown earlier in the spectral regions less than 1000 nm. All the device layers were grown at the same substrate temperature and laser intensity in a single vacuum PLD process, leading to a simplified large-area fabrication process.

Vanadium dioxide has been further utilized to design a plasmonic Yagi-Uda nanoantenna with the ability to switch its radiation beam between two directions opposite each other. The nanoantenna can dynamically switch the radiating beam in two directions opposite to each other. The plasmonic nanoantenna is optimized to radiate a similar amount of power with maximum signal-to-noise ratios in both the switching directions. The switching of the radiated beam is done by actively switching the phase of the VO₂ material used in the nanoantenna. The switching angle is also maximized to reduce the noise floor from the back lobe of radiation in other direction.

सार¹

नैनो-संरचित प्लास्मोनिक धातुओं को प्लास्मोनिक सेंसर और विभिन्न ऑप्टिकल उपकरणों में प्रगति के लिए बड़े पैमाने पर शोध किया गया है। नैनो-संरचित प्लास्मोनिक धातुएं हाइब्रिड सतह प्लाज्मा के उत्तेजना को सक्षम करती हैं, जिसमें लोकलाइज्ड और साथ ही प्रोपेगेटिंग सरफेस प्लास्मोन दोनों शामिल होते हैं। लोकलाइज्ड सरफेस प्लास्मोन आधारित उपकरणों का उपयोग आसपास के माध्यम में स्थानीय परिवर्तन का पता लगाने के लिए किया जा सकता है। नैनो-संरचित प्लास्मोनिक धातुएँ हमें प्रोपेगेटिंग सरफेस प्लास्मोन पोलरिटोन की युग्मन तकनीकों के साथ-साथ लोकलाइज्ड सरफेस प्लास्मों की पहचान क्षमताओं का उपयोग करने में सक्षम बनाती हैं।

संकीर्ण खांचा के साथ प्लास्मोनिक असमान नैनो-जाली पर आधारित एक सरफेस प्लास्मोन अनुनाद संवेदन और इमेजिंग प्लेटफॉर्म प्रस्तुत किया गया है। जब इन नैनो-जाली में मौजूद सोने की परत के आसपास के माध्यम के स्थानीयकृत अपवर्तक सूचकांक को बदल दिया जाता है, तो सैद्धांतिक विश्लेषण का उपयोग संख्यात्मक रूप से परावर्तन और अंतर परावर्तन संकेतों की गणना के लिए किया जाता है। सोने की परत के लिए जैव-अणुओं के बंधन से स्थानीयकृत अपवर्तक सूचकांक में परिवर्तन होगा। फाइनाईट डिफरेंस टाइम डोमेन मॉडलिंग का उपयोग प्लास्मोनिक असमान नैनो-जाली की जांच के लिए किया जाता है। ये प्लास्मोनिक असमान नैनो-जाली बहुत उच्च अंतर परावर्तन आयाम मान प्रदान करते हैं।

हम विभिन्न नैनो-संरचित प्लास्मोनिक सेंसर चिप्स का एक सैद्धांतिक अध्ययन भी प्रस्तुत करते हैं, जिसकी जांच उच्च संवेदनशीलता के साथ अत्यधिक संवेदनशील स्थानीयकृत संवेदन के लिए क्रेट्समैन कॉन्फिगरेशन का उपयोग करके दृश्यमान से अवरक्त तरंग दैर्ध्य तक की जाती है। प्रस्तावित नैनो-संरचित सेंसर चिप्स का विश्लेषण किया गया है, और कठोर युग्मित-लहर विश्लेषण पद्धति का उपयोग करके उनकी संवेदन क्षमता की तुलना की गयी है। नैनो-संरचनाओं की सतह पर जैव-अणुओं की एक पतली परत का पता लगाने पर ध्यान केंद्रित करने के लिए संवेदनशीलता मापदंडों को परिभाषित किया गया है। परावर्तकता मिनिमा में बदलाव सेंसर सतह पर स्थानीयकृत (स्थानीय बाध्यकारी विश्लेषण परत संवेदन) और थोक अपवर्तक सूचकांक (थोक मध्यम संवेदन) में गड़बड़ी के बारे में जानकारी प्राप्त करने के लिए निर्धारित किया जाता है। नैनो-संरचनाओं के आयाम और घटना कोण प्लास्मोन अनुनाद तरंगदैर्ध्य को स्थानांतरित करते हैं और ऑपरेटिंग तरंगदैर्ध्य को ट्यून करने के लिए इसका उपयोग किया जा सकता है। नैनो-संरचित फिल्मों उच्च विद्युत क्षेत्रों के स्थानीय क्षेत्रों का निर्माण करती हैं, जिसके परिणामस्वरूप प्रस्तावित संरचनाओं की संवेदनशीलता में वृद्धि होती है। इसके बाद हमने स्थानीय संवेदनशीलता को और बढ़ाने के लिए नैनो-संरचनाओं और पतली फिल्म के बीच एक स्पेसर पेश किया है। प्रस्तावित सेंसर को किसी भी परिष्कृत ऑप्टिकल सेट-अप की आवश्यकता नहीं होती है और इसे पारंपरिक क्रेट्समैन कॉन्फिगरेशन-आधारित सेंसर के लिए उपयोग किए जाने वाले ऑप्टिकल सेटअप पर लागू किया जा सकता

¹ यह मूल अंग्रेजी सार का अनुवादित संस्करण है। किसी भी विसंगति के मामले में अंग्रेजी संस्करण को प्राथमिकता दी जाएगी।

है। प्रस्तावित सेंसर डिजाइन को अत्याधुनिक टॉप-डाउन नैनोफाइब्रिकेशन दृष्टिकोणों का उपयोग करके आसानी से तैयार किया जा सकता है और अत्यधिक संवेदनशील जैव-संवेदन मंच विकसित करने के लिए नियोजित किया जा सकता है। एक ही माप में कई जैव-अणुओं का पता लगाने के लिए प्रस्तावित सेंसर का इस्तेमाल सरफेस प्लास्मोन रेजोनेंस इमेजिंग (एसपीआरआई) में किया जा सकता है।

आसपास के माध्यम में स्थानीय परिवर्तनों का पता लगाने के लिए प्लास्मोनिक नैनो-संरचनाओं की क्षमता का उपयोग प्लास्मोनिक स्विच को डिजाइन करने के लिए भी किया जाता है। हम VO_2 फिल्मों की परतों के बीच एम्बेडेड सोने के नैनोकणों (Au NPs) पर आधारित प्लास्मोनिक स्विच प्रस्तुत करते हैं। तापमान में परिवर्तन के साथ, वैनेडियम डाइऑक्साइड (VO_2) एक प्रतिवर्ती चरण परिवर्तन से गुजरता है, अर्धचालक से धातु तक। सोने के नैनोकणों के स्थानीयकृत सरफेस प्लास्मोन रेजोनेंस (एलएसपीआर) गुणों का उपयोग करके स्विचिंग डिवाइस के ऑपरेटिंग तरंग दैर्ध्य को 650 नैनोमीटर और 1000 नैनोमीटर के बीच ट्यून किया जा सकता है। हम प्रायोगिक रूप से और सैद्धांतिक रूप से एक उच्च स्विचेबिलिटी यानी VO_2 के चरण संक्रमण पर एक उच्च विलुप्त होने के अनुपात को प्रदर्शित करते हैं, जो पहले 1000 नैनोमीटर से कम वर्णक्रमीय क्षेत्रों में दिखाया गया है। सभी उपकरण परतें एक ही निर्वात पल्स लेज़र डेपोज़िशन प्रक्रिया में एक ही सबस्ट्रेट तापमान और लेजर तीव्रता पर उगाई गईं, जिससे एक सरल बड़े क्षेत्र की निर्माण प्रक्रिया हो गई।

वैनेडियम डाइऑक्साइड का उपयोग एक प्लास्मोनिक यागी-उडा नैनोएंटेना को एक दूसरे के विपरीत दो दिशाओं के बीच अपने विकिरण बीम को स्विच करने की क्षमता के साथ डिजाइन करने के लिए किया गया है। नैनोएंटेना गतिशील रूप से विकिरण बीम को एक दूसरे के विपरीत दो दिशाओं में स्विच कर सकता है। प्लास्मोनिक नैनोएंटेना दोनों स्विचिंग दिशाओं में अधिकतम सिग्नल-टू-शोर अनुपात के साथ समान मात्रा में बिजली विकीर्ण करने के लिए अनुकूलित है। विकिरणित बीम का स्विचिंग नैनोएंटेना में प्रयुक्त VO_2 सामग्री के चरण को सक्रिय रूप से स्विच करके किया जाता है। दूसरी दिशा में विकिरण के पीछे के लोब से शोर तल को कम करने के लिए स्विचिंग कोण को भी अधिकतम किया गया है।

Table of Contents

CERTIFICATE	i
ACKNOWLEDGEMENTS	ii
ABSTRACT	iii
संर	v
List of Abbreviation	x
List of Figures	xi
List of Tables	xxii
Chapter 1: Introduction	1
1.1 Overview	1
1.2 Propagating Surface Plasmon Resonance based Sensors.....	1
1.3 Localized Surface Plasmon Resonance based Sensors	3
1.4 Vanadium Dioxide (VO ₂) based devices	3
1.5 Thesis Outline	4
1.6 References	6
Chapter 2: Basic Plasmonics Theories and Literature Review	11
2.1 Metal Optical properties.....	11
2.2 Surface plasmon polariton.....	12
2.2.1 Kretschmann configuration and Otto configuration	14
2.2.2 Grating Coupling	15
2.3 Localized surface plasmons	16
2.4 Finite-difference time-domain method.....	18
2.5 Rigorous coupled-wave analysis.....	22
2.6 Surface plasmon based sensors	26
2.7 Phase change materials.....	28
2.8 Experimental Techniques for Thin Film Deposition and Characterization	29
2.8.1 Pulse Laser Deposition	29
2.8.2 X-Ray Diffraction	30
2.8.3 Spectroscopic Ellipsometry	31
2.8.4 Optical Measurement setup.....	31

Table of Contents

2.9	References	32
Chapter 3: Non-Uniform Narrow Groove Plasmonic Nano-Gratings for SPR Sensing and Imaging		35
3.0	Chapter Summery.....	35
3.1	Introduction	36
3.2	Numerical modeling using FDTD and RCWA	40
3.3	Results and Discussion.....	43
3.4	Conclusion.....	61
3.5	Appendix	61
3.6	References	63
Chapter 4: Nano-structured Plasmonic Chips employing Nanopillar and Nanoring Hole Arrays for Enhanced Sensitivity of SPR-based Biosensing		69
4.0	Chapter Summery.....	69
4.1	Introduction	69
4.2	Rigorous coupled wave analysis simulations.....	75
4.3	Results and discussion.....	77
4.4	Conclusion.....	87
4.5	References	88
Chapter 5: Enhanced SPR-based Localized and Bulk Sensing Using a Plasmonic Nanopillar Array with Spacer		93
5.0	Chapter Summery.....	93
5.1	Introduction	93
5.2	Sensor design and numerical modeling.....	96
5.3	Results and Discussion.....	99
5.4	Conclusion.....	111
5.5	Appendix	111
5.6	References	113
Chapter 6: Large-area plasmonic switches based on crystalline Au NPs between VO₂ layers for enhanced switching in Vis-NIR Regime.....		117
6.0	Chapter Summery.....	117
6.1	Introduction	117
6.2	Results and Discussion.....	121
6.2.1	Single Au NP layer stack.....	121

6.2.2	Simulation Results	128
6.2.3	Double Au NP layer stack	131
6.3	Conclusion.....	135
6.4	Methods	136
6.4.1	Fabrication	136
6.4.2	Characterization.....	136
6.4.3	Simulations	136
6.5	Appendix	137
6.6	References	140
Chapter 7: Dynamically Controlled Beam-switching of Plasmonic Yagi-Uda Nanoantenna		143
7.0	Chapter Summery.....	143
7.1	Introduction	143
7.2	Optical properties of VO ₂ material.....	144
7.3	Design and working principle of nanoantenna.....	145
7.4	Numerical Simulations.....	147
7.5	Results and Discussion.....	148
7.6	Conclusion.....	156
7.7	References	157
Chapter 8: Conclusions and suggestions for Future work.....		159
8.1	Conclusions	159
8.2	Suggestions for future work.....	161
Publications		163
BIODATA		165

List of Abbreviation

ALD: Atomic Layer Deposition
DALs: Double Au NP Layer Stack
DR: Differential Reflectance
EBL: e-beam Lithography
EM: Electromagnetic
FDTD: Finite-difference time-domain
FESEM: Field Emission Scanning Electron Microscope
FIB: Focused Ion Beam
FOM: Figure of Merit
FWHM: Full Width Half Maximum
GNG: Gold Nano-grating
GSNG: Gold-coated Silicon Nano-grating
IMIMI: Insulator-Metal-Insulator-Metal-Insulator
LSP: Localized surface plasmon
LSPR: Localized surface plasmon resonance
MIM: Metal-Insulator-Metal
PLD: Pulsed Laser Deposition
PML: Perfectly Matched Layer
PSP: Propagating Surface Plasmon
RCWA: Rigorous coupled-wave Analysis
RIE: Reactive Ion Etching
SALS: Single Au NP Layer Stack
SERS: Surface-enhanced Raman scattering
SNR: Signal-to-Noise Ratio
SP: Surface plasmon
SPP: Surface Plasmon Polariton
SPRi: Surface Plasmon Resonance Imaging
XRD: X-ray Diffraction

List of Figures

Fig. 2.1. (a) The schematic shows SPP propagation along the x-axis on a metal-dielectric interface, as well as the transverse magnetic characteristic of SPPs. (b) The exponential decay of the SPPs' z-components away from the interface. δ_m and δ_d are the SPPs' penetration depths in metal and dielectric, respectively. Reprinted from the ref. [3].	12
Fig. 2.2. Dispersion relation of SPPs at a metal-dielectric interface formed between the metal of negligible damping and a dielectric.	13
Fig. 2.3. The Schematic of SPPs coupling through (a) Otto configuration and (b) Kretschmann configuration.	14
Fig. 2.4. Phase matching technique to couple SPPs at the metal-dielectric interface using prism coupling.	15
Fig. 2.5. Phase matching technique to couple SPPs at the metal-dielectric interface using grating.	16
Fig. 2.6. Absorbance spectrum for binding events on nanoparticles is shown, and visualization of the localized surface plasmon.	17
Fig. 2.7. A representation of Yee's cell with electric fields at the edges and magnetic fields at the faces.	20
Fig. 2.8. (a) Three-dimensional model of the diffraction grating with the region of interest. (b) The diagram illustrates how the RCWA eliminates the z dependence [7].	23
Fig. 2.9. SPR measurement employing the Kretschmann configuration before and after the presence of the analyte, demonstrating a spectrum shift at the detector [16].	26
Fig. 2.10. The real and imaginary part of the refractive index of VO ₂ at low temperature (LT) and at high temperature (HT).	28
Fig. 2.11. Schematic of a Pulsed Laser Deposition system.	30
Fig. 2.12. Schematic of optical setup developed for the characterization of plasmonic chips in transmission mode.	31

- Fig. 3.1.** (a) The Kretschmann configuration for a 40 nm gold film. (b) A schematic showing a cross-sectional view of non-uniform gold-coated silicon nano-gratings (GSNG)..... 37
- Fig. 3.2.** Schematic diagrams illustrating different types of nano-gratings: (a) uniform rectangular aperture nano-gratings, (b) non-uniform gold nano-gratings (GNGs), and (c) gold-coated silicon nano-gratings (GSNGs). H and P represent the height and periodicity of the nanogratings, respectively. The groove width is denoted by W and is calculated at a height $H/2$ from the bottom of the nano-grating. (d) SEM/TEM cross-section of gold-coated silicon nano-gratings over-coated with hafnium oxide (HfO_2) layer for smooth deposition of metallic gold film and reducing gaps between adjacent silicon nano-grating structures [45]. 43
- Fig. 3.3.** (a) RCWA simulations of a 40 nm thick continuous gold film employing the Kretschmann configuration, (b) Results of FDTD simulations for GNGs, and (c) Results of FDTD simulations for GSNGs showing the reflectance spectra and differential reflectance spectra. Geometrical parameters for the non-uniform nanogratings are periodicity $P = 200$ nm, height $H = 200$ nm, and groove width $W = 16.5$ nm..... 45
- Fig. 3.4.** FDTD simulation results showing the spatial distribution of E-field enhancement (E/E_0) in non-uniform gold nano-gratings for an excitation wavelength of (a) 1180 nm (off-resonance) and (b) 950 nm (on-resonance). Geometrical parameters for these non-uniform gold nano-gratings are periodicity $P = 200$ nm, height $H = 200$ nm, and groove width $W = 16.5$ nm. FDTD simulation results showing the spatial distribution of E-field enhancement in non-uniform gold-coated silicon nano-gratings for an excitation wavelength of (c) 1500 nm (off-resonance) and (d) 1090 nm (on-resonance). The geometrical parameters for these non-uniform nano-gratings are periodicity $P = 250$ nm, height $H = 200$ nm, and groove width $W = 20.625$ nm..... 46
- Fig. 3.5.** FDTD simulation results showing reflectance spectra and DR spectra for: (a) uniform rectangular aperture gold nano-gratings, (b) non-uniform gold nano-gratings (GNGs), and (c) non-uniform gold-coated silicon nano-gratings (GSNGs). The geometrical parameters for these nano-gratings are periodicity $P = 100$ nm, height $H = 200$ nm, and groove width $W = 8.25$ nm. 48
- Fig. 3.6.** FDTD simulation results showing reflectance spectra and DR spectra for GNGs, for several nano-grating heights H : (a) 100 nm (b) 200 nm (c) 250 nm and (d) 300 nm. The other geometrical parameters for these nano-gratings are groove width $W = 16.5$ nm and periodicity $P = 200$ nm..... 49
- Fig. 3.7.** FDTD simulation results showing reflectance spectra and DR spectra for GSNGs, for several nano-grating heights H : (a) 100 nm (b) 200 nm (c) 250 nm and (d) 300 nm.

- The other geometrical parameters for these nano-gratings are groove width $W = 16.5$ nm and periodicity $P = 200$ nm..... 51
- Fig. 3.8.** FDTD simulation results showing reflectance spectra and DR spectra for GNGs, for several nano-grating groove widths W : (a) 8.25 nm, (b) 12.375 nm, (c) 16.5 nm, and (d) 24.75 nm. The other geometrical parameters for these nano-gratings are height $H = 200$ nm and periodicity $P = 200$ nm..... 52
- Fig. 3.9.** FDTD simulation results showing reflectance spectra and DR spectra for GSNGs, for several nano-grating groove widths W : (a) 8.25 nm, (b) 12.375 nm, (c) 16.5 nm, and (d) 24.75 nm. The other geometrical parameters for these nano-gratings are height $H = 200$ nm and periodicity $P = 200$ nm..... 53
- Fig. 3.10.** FDTD simulation results showing the effect of change in: (a) Height, and (b) Periodicity on the biosensing performance of the GNGs and GSNGs. 60
- Fig. 4.1.** (a) Schematic of nano-structured plasmonic sensor chip, consisting of plasmonic nano-structures present on the surface of a plasmonic (Au) thin film, interrogated using the Kretschmann configuration with a 1 nm layer (red color) on top of the nano-structure. (b) xy-map of the E-field profile in the resonance condition for a nano-structured plasmonic thin film. (c) Differential reflectance spectra and reflectance spectra of a nano-structured plasmonic thin film in the presence and in the absence of the bio-layer. Schematic diagrams showing different configurations of the nano-structured plasmonic sensor chips: (d) a cylindrical nanopillar array, (e) a cylindrical nanoring hole array, (f) a diamond nanopillar array, and (g) a diamond nanoring hole array present on top of a 40 nm gold film and interrogated using the Kretschmann configuration. 71
- Fig. 4.2.** Reflectance and differential reflectance spectra of a: (a) Cylindrical Nanopillar array, (b) Cylindrical Nanoring hole array, (c) Diamond Nanopillar array, and (d) Diamond Nanoring hole array present on top of a 40 nm gold film and interrogated using the Kretschmann configuration. The reflectance spectra are calculated for both presence and absence of bio-layer. The values of $h_1 = 40$ nm, $h_2 = 40$ nm, $d = 40$ nm and $g = 5$ nm for all structures. 76
- Fig. 4.3.** E-field profiles for a cylindrical nanopillar array present on top of a 40 nm gold film and interrogated using the Kretschmann configuration calculated for: (a) on-resonance condition and (b) off-resonance condition. E-field profiles for a cylindrical nanoring hole array present on top of a 40 nm gold film calculated for: (c) on-resonance condition and (d) off-resonance condition. E-field profiles for a diamond nanopillar array present on top of a 40 nm gold film calculated for: (e) on-resonance condition and (f) off-resonance condition. E-field profiles for a diamond nanoring hole array

present on top of a 40 nm gold film calculated for: (g) on-resonance condition and (h) off-resonance condition. The values of $h_1 = 40$ nm, $h_2 = 40$ nm, $d = 40$ nm, and $g = 5$ nm for all structures. 78

Fig. 4.4. Angulo-spectral map showing reflectance from nanopillar arrays present on top of a thin gold film without any biolayer for: (a) a cylindrical nanopillar array and (e) a diamond nanopillar array. Angulo-spectral map showing reflectance from nanopillar arrays present on top of a thin gold film with a biolayer covering the surface of the nano-structures and the gold film for: (b) a cylindrical nanopillar array and (f) a diamond nanopillar array. Angulo-spectral maps showing differential reflectance for: (c) cylindrical nanopillar arrays and (g) diamond nanopillar arrays present on top of a gold film. The values of $h_1 = 40$ nm, $h_2 = 40$ nm and $g = 5$ nm for all structures. The values of d for the cylindrical nanopillar array and the diamond nanopillar array are 60 nm and 40 nm, respectively. Schematic diagrams of the nanopillar arrays present on top of gold films are shown for: (d) the cylindrical nanopillar array and (h) the diamond nanopillar array. 80

Fig. 4.5. Angulo-spectral map showing reflectance from nanoring hole arrays present on top of a thin gold film without any biolayer for: (a) a cylindrical nanoring hole array and (e) a diamond nanoring hole array. Angulo-spectral map showing reflectance from nanoring hole arrays present on top of a thin gold film with a biolayer covering the surface of the nano-structures and the gold film for: (b) a cylindrical nanoring hole array and (f) a diamond nanoring hole array. Angulo-spectral maps showing differential reflectance for: (c) cylindrical nanoring hole arrays and (g) diamond nanoring hole arrays present on top of a gold film. The values of $h_1 = 40$ nm, $h_2 = 40$ nm and $g = 5$ nm for all structures. The values of d for the cylindrical nanoring hole array and the diamond nanoring hole array are 60 nm and 40 nm, respectively. Schematic diagrams of the nanoring hole arrays present on top of gold films are shown for: (d) the cylindrical nanoring hole array and (h) the diamond nanoring hole array..... 81

Fig. 4.6. Effect of variation in parameter ‘ g ’ on the values of the surface sensitivity (S_S) and maximum differential reflectance (DR_{Max}) for different configurations of the nano-structures present on top of a thin gold film: (a) & (c) a cylindrical nanopillar array and a diamond nanopillar array and (b) & (d) a cylindrical nanoring hole array and a diamond nanoring hole array. For comparison, the maximum differential reflectance for an optimized plain gold film is also shown in the figures with a dashed line. The values of both h_2 and d are taken as 40 nm. 82

Fig. 4.7. Effect of variation in parameter, ‘ h_2 ’ on the values of the surface sensitivity (S_S) and maximum differential reflectance (DR_{Max}) for different configurations of the nano-structures present on top of a thin gold film: (a) & (c) a cylindrical nanopillar array

and a diamond nanopillar array and (b) & (d) a cylindrical nanoring hole array and a diamond nanoring hole array. For comparison, the maximum differential reflectance for an optimized plain gold film is also shown in the figures with a dashed line. The values of d and g are taken as 50 nm and 5 nm, respectively. 84

Fig. 5.1. (a) Schematic representation of the proposed plasmonic sensor in a bulk sensing medium in perspective view. (b) 2D depiction of the sensor showing localized sensing biomolecular binding layer in red color. Several geometrical parameters of the structure are denoted: diameter of nanopillar, D ; spacer diameter, d ; gold film thickness, H_{Au} , nanopillar height, H , spacer thickness, t ; and interpillar gap, g ; shape dependence parameter of the metal nanopillar, $R (= d_2/d_1)$, d_1 and d_2 are the longitudinal and lateral diameters of the elliptical metal nanopillar. The proposed sensor employs a SF10 glass prism with a refractive index of 1.715. An adhesion layer of 1 nm titanium between the glass prism and the gold film is shown in purple color. (c) Spectral interrogation reflectance response at 75° incidence angle showing spectral shift due to refractive index variations caused by the biomolecular binding layer. (d) Angular interrogation reflectance response at 1024 nm showing angular shift due to refractive index variations caused by the biomolecular binding layer. (E) Angle-dependent spectral reflectance color maps showing the effect of adsorbed biolayer. The dimensions of the plasmonic sensor are: $H_{Au} = 40$ nm, $t = 10$ nm, $g = 5$ nm, $d = 25$ nm, $D = 50$ nm, $H = 20$ nm, aspect ratio dimension of nanopillar, $R = 1$, index of spacer, $n_s = 1.5$. The thickness of the biomolecular binding layer was taken to be 1 nm..... 98

Fig. 5.2. Evaluation of localized sensitivity parameters using angulo-spectral interrogation of the sensor: (a) Sensitivity parameters for spectral interrogation of the localized sensor. (b) Sensitivity parameters for angular interrogation of the localized sensor. The dimensions of the plasmonic sensor were taken to be: $H_{Au} = 40$ nm, $t = 10$ nm, $g = 5$ nm, $d = 25$ nm, $D = 50$ nm, $H = 20$ nm, aspect ratio dimension of nanopillar, $R = 1$, index of spacer, $n_s = 1.5$ 100

Fig. 5.3. E-field distribution for spectral interrogation ($\theta = 75^\circ$) in the off-resonance condition at $\lambda = 1500$ nm (row 1) and in the on-resonance condition at $\lambda = 1000$ nm (row 2) in the: (a), (d) XZ plane of the structure; (b), (e) XY plane where the cylindrical spacer thickness is $t/2$; (c), (f) XY plane where the nanopillar height is $H/2$. E-field distribution for angular interrogation ($\lambda = 1024$ nm) in the off-resonance condition at $\theta = 55^\circ$ (row 3) and in the on-resonance condition at $\theta = 70^\circ$ (row 4) in the: (g), (j) XZ plane of the structure; (h), (k) XY plane where the cylindrical spacer thickness is $t/2$; (i), (l) XY plane where the nanopillar height is $H/2$. The dimensions of the plasmonic sensor were taken to be: $H_{Au} = 40$ nm, $t = 10$ nm, $g = 5$ nm, $d = 25$ nm, $D = 50$ nm, $H = 20$ nm, aspect ratio dimension of nanopillar, $R = 1$, index of spacer, $n_s = 1.5$ 102

- Fig. 5.4.** Effect of variation of spacer thickness t , on bulk and localized sensing parameters: (a) Wavelength-interrogation surface sensitivity and FOM with variation in t . (b) Wavelength-interrogation bulk sensitivity and FOM variation with t . (c) Angle dependent spectral reflectance color plots showing variation of reflection band corresponding to plasmon related reflection dips with change in t plotted for three discrete values of t . The other dimensions of the plasmonic sensor were taken to be: $H_{Au} = 40$ nm, $g = 5$ nm, $d = 25$ nm, $D = 50$ nm, $H = 20$ nm, and aspect ratio dimension of nanopillar, $R = 1$, index of spacer, $n_s = 1.5$ 104
- Fig. 5.5.** E-field distribution profiles for structures without dielectric spacers. E-field distribution for spectral interrogation ($\theta = 75^\circ$) in the off-resonance condition at $\lambda = 1500$ nm (row 1) and in the on-resonance condition at $\lambda = 800$ nm (row 2) in the: (a), (d) XZ plane of the structure; (b), (e) XY plane on surface $z = 0$; (c), (f) XY plane where nanopillar height is $H/2$. The dimensions of the plasmonic sensor were taken to be: $H_{Au} = 40$ nm, $t = 0$ nm, $g = 5$ nm, $d = 25$ nm, $D = 50$ nm, $H = 20$ nm, aspect ratio dimension of nanopillar, $R = 1$, and index of spacer, $n_s = 1.5$ 105
- Fig. 5.6.** Effect of variation of nanopillar gap, g , on bulk and localized sensing parameters: (a) Wavelength-interrogation surface sensitivity and FOM with variation in g . (b) Wavelength-interrogation bulk sensitivity and FOM with variation in g . (c) Angle dependent spectral reflectance color plots showing variation of reflection band corresponding to plasmon related reflection dips with change in g plotted for three discrete values of g . The other dimensions of the plasmonic sensor were taken to be: $H_{Au} = 40$ nm, $t = 10$ nm, $d = 25$ nm, $D = 50$ nm, $H = 20$ nm, aspect ratio dimension of nanopillar, $R = 1$, index of spacer, $n_s = 1.5$ 106
- Fig. 5.7.** Effect of variation of nanopillar diameter, D , on bulk and localized sensing parameters: (a) Wavelength-interrogation surface sensitivity and FOM with variation in D . (b) Wavelength-interrogation bulk sensitivity and FOM variation with D . (c) Angle dependent spectral reflectance color plots showing variation of reflection band corresponding to plasmon related reflection dips with change in D plotted for three discrete values of D . The other dimensions of the plasmonic sensor were taken to be: $H_{Au} = 40$ nm, $t = 10$ nm, $g = 5$ nm, $d = 25$ nm, $H = 20$ nm, aspect ratio dimension of nanopillar, $R = 1$, index of spacer, $n_s = 1.5$ 107
- Fig. 5.8.** Effect of variation of nanopillar height, H , on bulk and localized sensing parameters: (a) λ -interrogation surface sensitivity and FOM variation with H . (b) θ -interrogation surface sensitivity and FOM variation with H . (c) Angle dependent spectral reflectance color plots showing variation of reflection band corresponding to plasmon related reflection dips with change in H plotted for three discrete values of H . The other dimensions of the plasmonic sensor were taken to be: $H_{Au} = 40$ nm, $t = 10$ nm, g

- $= 5 \text{ nm}$, $d = 25 \text{ nm}$, $D = 50 \text{ nm}$, aspect ratio dimension of nanopillar, $R = 1$, index of spacer, $n_s = 1.5$ 108
- Fig. 5.9.** Effect of variation of the aspect ratio of metallic nanopillar, R , on bulk and localized sensing parameters: (a) Wavelength-interrogation surface sensitivity and FOM with variation in R . (b) Wavelength-interrogation bulk sensitivity and FOM variation with R . (c) Angle dependent spectral reflectance color plots showing variation of reflection band corresponding to plasmon related reflection dips with change in R plotted for three discrete values of R . The other dimensions of the plasmonic sensor were taken to be: $H_{Au} = 40 \text{ nm}$, $t = 10 \text{ nm}$, $g = 5 \text{ nm}$, $d = 25 \text{ nm}$, $D = 50 \text{ nm}$, $H = 20 \text{ nm}$, index of spacer, $n_s = 1.5$ 109
- Fig. 5.10.** Effect of variation of spacer index, n_s on bulk and localized sensing parameters. (a) Wavelength-interrogation surface sensitivity and FOM variation with n_s . (b) Wavelength-interrogation bulk sensitivity and FOM variation with n_s . (c) Angle dependent spectral reflectance color plots showing variation of reflection band corresponding to plasmon related reflection dips with change in n_s plotted for three discrete values of n_s . The dimensions of the plasmonic sensor were taken to be: $H_{Au} = 40 \text{ nm}$, $t = 10 \text{ nm}$, $g = 5 \text{ nm}$, $d = 25 \text{ nm}$, $D = 50 \text{ nm}$, $H = 20 \text{ nm}$, and aspect ratio dimension of nanopillar, $R = 1$ 111
- Fig. 5.11.** Effect of variation of spacer index, d on bulk and localized sensing parameters. (a) Wavelength-interrogation surface sensitivity and FOM variation with d . (b) Wavelength-interrogation bulk sensitivity and FOM variation with d . (c) Angle dependent spectral reflectance color plots showing variation of reflection band corresponding to plasmon related reflection dips with change in n_s plotted for three discrete values of d . The other dimensions of the plasmonic sensor were taken to be: $H_{Au} = 40 \text{ nm}$, $t = 10 \text{ nm}$, $g = 5 \text{ nm}$, $D = 50 \text{ nm}$, $H = 20 \text{ nm}$, aspect ratio dimension of nanopillar, $R = 1$, and index of spacer, $n_s = 1.5$ 112
- Fig. 5.12.** Effect of variation of gold film thickness, H_{Au} on bulk and localized sensing parameters. (a) Wavelength-interrogation surface sensitivity and FOM variation with H_{Au} . (b) λ -interrogation bulk sensitivity and FOM variation with H_{Au} . (c) Angle dependent spectral reflectance color plots showing variation of reflection band corresponding to plasmon related reflection dips with change in H_{Au} plotted for three discrete values of H_{Au} . The other dimensions of the plasmonic sensor were taken to be: $t = 10 \text{ nm}$, $g = 5 \text{ nm}$, $d = 25 \text{ nm}$, $D = 50 \text{ nm}$, $H = 20 \text{ nm}$, aspect ratio dimension of nanopillar, $R = 1$, index of spacer, $n_s = 1.5$ 112
- Fig. 6.1.** Schematic of a fabricated: (a) ‘single Au NP layer’ stack and (b) ‘double Au NP layer’ stack employed for optical switching. (c) SEM image of the Au nanoparticles on a VO_2 film when 8000 laser pulses were employed for the nanoparticle formation. (d)

- Schematic of the optical setup employed for measuring the transmission spectra of the fabricated chips. 120
- Fig. 6.2.** Normalized transmission spectra for a ‘single Au NP layer’ stack at LT (25 °C) and HT (90 °C) are shown for the different number (N_{Au}) of laser pulses employed for Au NP formation, i.e. for N_{Au} : (a) Zero, (b) 1000, (c) 3000, (d) 5000, and (e) 8000. (f) Extinction ratio of the plasmonic switch for different values of N_{Au} . The bottom and top VO₂ layers were deposited with N_{VO_2} (Bottom) = 12000 and N_{VO_2} (Top) = 6000 laser pulses. 123
- Fig. 6.3.** Absorption spectra for a ‘single Au NP layer’ stack at LT (25 °C) and HT (90 °C) are shown for the different number (N_{Au}) of laser pulses employed for Au NP formation, i.e. for N_{Au} : (a) 5000, and (b) 8000. The bottom and top VO₂ layers were deposited with N_{VO_2} (Bottom) = 12000 and N_{VO_2} (Top) = 6000 laser pulses. 124
- Fig. 6.4.** Schematic of the Pulsed Laser Deposition (PLD) system used for the growth of VO₂ thin film and the growth of Au NPs. Scanning electron microscopy (SEM) images of the Au NPs on VO₂ film for different number of laser pulses employed for Au NP formation, i.e. for N_{Au} : (b) Zero — VO₂ thin film, (c) 1000, (d) 3000, (e) 5000, and (f) 8000. 126
- Fig. 6.5.** Thermal hysteresis loop of a normalized transmission measured at a wavelength of 830 nm for a VO₂ thin film (dotted) and a ‘single Au NP layer’ stack with $N_{Au} = 8000$ pulses (solid). The bottom and top VO₂ layers were deposited with N_{VO_2} (Bottom) = 12000 and N_{VO_2} (Top) = 6000 laser pulses. While N_{Au} is the number of laser pulses employed for Au NP formation, N_{VO_2} (Top) and N_{VO_2} (Bottom) are the number of laser pulses employed for the formation of the top VO₂ thin film layer and the bottom VO₂ thin film layer, respectively. 127
- Fig. 6.6.** (a) Schematic of the ‘single Au NP layer’ stack studied using FDTD simulations. Results of FDTD simulations showing the normalized transmission at (b) LT (25 °C) and (c) HT (90 °C). (d) Extinction ratio of the plasmonic switch for different diameters, d of Au NPs. E-field distribution for $d = 26$ nm along the XZ plane at (e) LT and (f) HT at 860 nm. E-field distribution for $d = 26$ nm along XY plane at (g) LT and (h) HT at 860 nm. 129
- Fig. 6.7.** Schematic of the ‘multiple Au NP layer’ stacks studied using FDTD simulations. Results of FDTD simulations showing the normalized transmission at (b) LT (25 °C) and (c) HT (90 °C). (d) Extinction ratio of the plasmonic switch for increasing number of the Au NP layers, n 130

- Fig. 6.8.** Normalized transmission spectra of ‘double Au NP layer’ stack (DALs) at LT (25 °C) and HT (90 °C) are shown for different middle VO₂ layer deposition pulses, N_{VO_2} (Mid): (a) 1000, (b) 4000, and (c) 8000. (d) Extinction ratio of the plasmonic switch for different middle VO₂ layer deposition pulses. The dashed lines represent the characteristics for the ‘single Au NP layer’ stack (SALS) with laser pulses, $N_{Au} = 5000$. The bottom and top VO₂ layers were deposited with N_{VO_2} (Bottom) = 12000 and N_{VO_2} (Top) = 6000 laser pulses. Au NPs were grown with N_{Au} (Top) = N_{Au} (Bottom) = 5000 laser pulses. While N_{Au} is the number of laser pulses employed for Au NP formation in SALS, N_{Au} (Top) and N_{Au} (Bottom) are the number of laser pulses employed for Au NP formation in the top and bottom Au NP layers, respectively, in DALs. N_{VO_2} (Top), N_{VO_2} (Mid), and N_{VO_2} (Bottom) are the number of laser pulses employed for the formation of the top VO₂ layer, the middle VO₂ layer, and the bottom VO₂ layer, respectively, in DALs. 132
- Fig. 6.9.** Thermal hysteresis loop at wavelengths (a) 690 nm, (b) 785 nm, (c) 830 nm, and (d) 880 nm for VO₂ thin film (dotted) and respective ‘double Au NP layer’ stacks (solid). The bottom and top VO₂ layers were deposited with N_{VO_2} (Bottom) = 12000 and N_{VO_2} (Top) = 6000 laser pulses. Au NPs were grown with N_{Au} (Top) = N_{Au} (Bottom) = 5000 laser pulses. While N_{Au} is the number of laser pulses employed for Au NP formation, N_{VO_2} (Top), N_{VO_2} (Mid), and N_{VO_2} (Bottom) are the number of laser pulses employed for the formation of the top VO₂ thin film layer, the middle VO₂ thin film layer, and the bottom VO₂ thin film layer, respectively. 134
- Fig. 6.10.** Real (n) and imaginary (k) refractive indices of the grown VO₂ thin film — as a function of wavelength — at LT (25°C) and HT (90°C), measured using spectroscopic ellipsometry..... 137
- Fig. 6.11.** XRD pattern of VO₂ thin film (18000 laser pulses) on c-plane sapphire..... 137
- Fig. 6.12.** Histogram plots of the Au nanoparticle size distributions for different Au deposition pulses, N_{Au} : (a) 1000, (b) 3000, (c) 5000, and (d) 8000. 138
- Fig. 6.13.** Results of FDTD simulations showing the normalized transmission of Au NP with different diameter (d) on top of the sapphire substrate. 139
- Fig. 6.14.** XRD pattern of a ‘double Au NP layer’ stack showing both Au and VO₂ peaks. 139
- Fig. 7.1.** The effect of phase transition of VO₂ on the values of (a) real part (ϵ_1) and (b) imaginary part (ϵ_2) of the dielectric constant of the material [16]. 145
- Fig. 7.2.** (a) Antenna Radiation pattern at an angle θ . (b) Schematic of Yagi-Uda nanoantenna inside SiO₂ material. The height (in the z-direction) of reflector, feed element, and

director is 50 nm each. The width (in the x-direction) of reflector and director is 25 nm each. The width of feed elements is 35 nm total (25 nm VO₂, 10 nm Au). QD: Quantum Dipole. 146

Fig. 7.3. Far-field radiation intensity pattern for the (a) semiconductor and (b) metallic state of VO₂ for the nanoantenna having only feed element. The circular rings in the pattern represent the different values of elevation angle ‘ θ ,’ and one complete circle represents a variation of zero to 360° of azimuth angle ‘ ϕ ’. Far-field radiation pattern calculated for the nanoantenna having only feed element calculated in the direction of the maximum radiation intensity ($\theta = 0^\circ$). (d) Schematic of designed nanoantenna having only feed element. Note that the intensity values in (c) are normalized by dividing by 10^{-12} 148

Fig. 7.4. Effect of variation in the length of the reflector (Rl) and director (Dl) (a) on SNR of metallic state radiation (Ψ_m), (b) on SNR of semiconductor state radiation (Ψ_s), and (c) on the FOM (Ω). Effect of variation in spacing between the reflector and feed element (Rs) and spacing between director and feed element (Ds) (d) on SNR of metallic state radiation (Ψ_m), (e) on SNR of semiconductor state radiation (Ψ_s), and (f) on the FOM (Ω). 149

Fig. 7.5. Effect on the switching angle between the direction of radiation beams of two states with a variation (a) in the length of reflector (Rl) and director (Dl), and (b) in spacing between the reflector and feed element (Rs) and spacing between the director and feed element (Ds). 151

Fig. 7.6. Far-field radiation patterns calculated for the optimized nanoantenna for high values of Ω . Dashed blue plots are the radiation pattern of the semiconductor state of VO₂ in the direction of the maximum radiation intensity of the metallic state. Dashed red plots are the radiation pattern of the metallic state of VO₂ in the direction of the maximum radiation intensity of the semiconductor state. Note that the intensity values in (c) are normalized by dividing by 10^{-12} 152

Fig. 7.7. The near-field radiation pattern of the nanoantenna in (a) metallic and (e) semiconductor states. The near-field radiation pattern of the three polarisations of e-field (b) E_x , (c) E_z , and (d) E_y are shown for the metallic state. The near-field radiation pattern of the three polarisations of e-field (f) E_x , (g) E_z , and (h) E_y are shown for the semiconductor state. The lengths of the reflector and director are 210 nm and 160 nm, respectively. The distances of reflector and director from feed element are 50 nm and 80 nm, respectively. 153

Fig. 7.8. Far-field radiation intensity pattern for the (a) semiconductor and (b) metallic phase of VO₂. The circular rings in the pattern represent the different values of elevation angle

‘ θ ,’ and one complete circle represents a variation of zero to 360° of azimuth angle ‘ ϕ ’. Far-field radiation pattern calculated for the optimized nanoantenna with highest SNR values (c) for metallic state at $\theta = \theta_m = 40^\circ$, and (d) for semiconductor state at $\theta = \theta_s = 36^\circ$. Note that the intensity values in (c) are normalized by dividing by 10^{-12} 155

Fig. 7.9. 3D far-field radiation pattern of the plasmonic nanoantenna (a) for semiconductor state, (b) for the metallic state, and (c) for both states of VO₂. Schematic of Yagi-Uda nanoantenna inside SiO₂ material. The dimensional parameters of nanoantenna are $Rl = 210$ nm, $Dl = 160$ nm, $Rs = 50$ nm and $Ds = 80$ nm. 156

List of Tables

Table 3.1. DR_{AMP} values for GNGs with $W = 8.25$ nm	54
Table 3.2. DR_{AMP} values for GSNGs with $W = 8.25$ nm.....	55
Table 3.3. DR_{AMP} values for GNGs and GSNGs with $P = 200$ nm and $H = 200$ nm.....	55
Table 3.4. S_S (in nm/nm) for GNGs with $W = 8.25$ nm.....	56
Table 3.5. S_S (in nm/nm) for GSNGs with $W = 8.25$ nm	56
Table 3.6. S_S (in nm/nm) for GNGs and GSNGs with $P = 200$ nm and $H = 200$ nm	57
Table 3.7. FOM_S (in nm^{-1}) for GNGs with $W = 8.25$ nm.....	57
Table 3.8. FOM_S (in nm^{-1}) for GSNGs with $W = 8.25$ nm.....	58
Table 3.9. FOM_S (in nm^{-1}) for GNGs and GSNGs with $P = 200$ nm and $H = 200$ nm.....	58
Table 3.10. Surface and Bulk sensitivities of different plasmonic sensors.....	59
Table 4.1. FOM_S (in nm^{-1}) values for four nano-structured thin films with the variation in parameter ‘ g ’. The values of both h_2 and d are taken as 40 nm.	83
Table 4.2. FOM_S (in nm^{-1}) values for four nano-structured thin films with the variation in parameter ‘ h_2 ’. The values of d and g are taken as 50 nm and 5 nm, respectively.	85
Table 4.3. Surface sensitivity of different plasmonic sensors.....	86
Table 5.1. Comparison of localized and bulk sensing response of the proposed sensor with published Literature	110